ACS Photonics

pubs.acs.org/journal/apchd5 Article

Ultrafast Quantum-Well Photodetectors Operating at 10 μm with a Flat Frequency Response up to 70 GHz at Room Temperature

Michael Hakl,[‡] Quyang Lin,[‡] Sylvie Lepillet, Maximilien Billet, Jean-François Lampin, Stefano Pirotta, Raffaele Colombelli, Wenjian Wan, J. C. Cao, Hua Li, Emilien Peytavit, and Stefano Barbieri*

Cite This: *ACS Photonics* 2021, 8, 464–471 Read Online

ACCESS | Metrics & More | Article Recommendations | Supporting Information

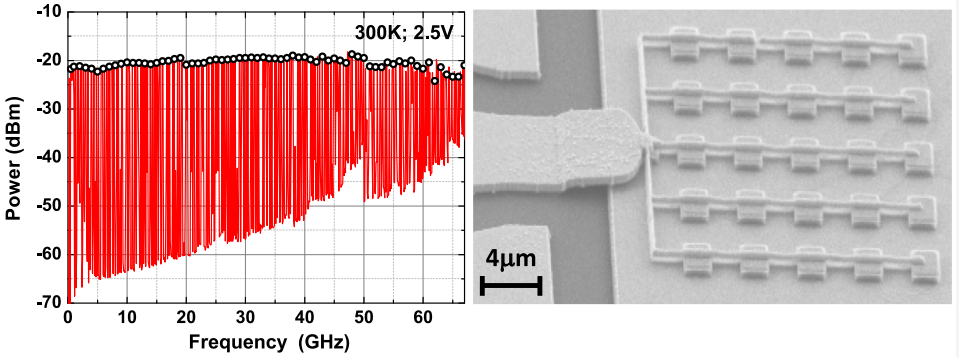

ABSTRACT: III−V semiconductor mid-infrared photodetectors based on intersubband transitions hold great potential for ultrahigh-speed operation up to several hundreds of GHz. In this work we exploit a ∼350 nm thick GaAs/$Al_{0.2}Ga_{0.8}As$ multi-quantum-well heterostructure to demonstrate heterodyne detection at $\lambda \sim 10$ μm with a nearly flat frequency response up to 70 GHz at room temperature, solely limited by the measurement system bandwidth. This is the broadest RF-bandwidth reported to date for a quantum-well mid-infrared photodetector. Responsivities of 0.15 and 1.5 A/W are obtained at 300 and 77 K. respectively. To allow ultrafast operation and illumination at normal incidence, the detector consists of a 50Ω coplanar waveguide, monolithically integrated with a 2D array of subwavelength patch antennas, electrically interconnected by suspended wires. With this device architecture, we obtain a parasitic capacitance of ∼30 fF, corresponding to the static capacitance of the antennas, yielding a RC-limited 3 dB cutoff frequency >150 GHz at 300 K, extracted with a small-signal equivalent circuit model. Using this model, we quantitively reproduce the detector frequency response and find intrinsic roll-off time constants as low as 1 ps at room temperature.

KEYWORDS: *mid-infrared, quantum-well photodetector, intersubband transitions, infrared antenna, heterodyne detection, broadband*

Thanks to their intrinsically short electron relaxation time, on the ps time scale, mid-infrared (MIR-3−12 μm) quantum-well infrared photodetectors (QWIP) based on III−V semiconductor materials were identified as ideal candidates for ultrahigh-speed operation at the end of the 80s. Since then, several experiments have been carried out to determine their RF bandwidth using both pulsed mid-infrared excitation or heterodyne detection.[1−7]

The exploitation of QWIPs as heterodyne receivers with IF bandwidth of tens of GHz is particularly attractive for a number of applications, including free-space communications, gas sensing and spectroscopy, atmospheric and space science, and so on.[8−11] Besides enabling the implementation of coherent detection schemes, another advantage brought by heterodyne detection is the possibility to operate QWIPs in the shot-noise regime, overcoming the noise contribution of the thermally activated dark current, which severely impacts the NEP of MIR QWIPs at high temperature.[12] So far, the largest heterodyne detection bandwidths at room temperature are those obtained by Grant et al. using a 100 quantum wells (QWs) QWIP operating at 10 μm.[6,7] The device was processed in a 16 μm side square mesa, illuminated from a 45° polished substrate, which is not practical for applications. At room temperature, a ∼25 GHz 3 dB cutoff and ∼10 dB attenuation at 110 GHz were demonstrated, clearly illustrating the high frequency potential of QWIPs.

In the context of high-speed QWIPs, the possibility of coupling the detector element to an antenna opens interesting perspectives. Indeed, the antenna allows a reduction of the detector active volume without sacrificing the radiation

Received: August 18, 2020
Published: January 29, 2021

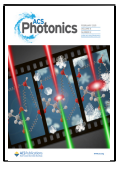

https://dx.doi.org/10.1021/acsphotonics.0c01299
ACS Photonics 2021, 8, 464−471

collection area, thus, avoiding a reduction of the quantum efficiency. Nanoantennas were first applied to MIR bolometers as a way to increase both their sensitivity and their speed.[13−15] QWIPs based on arrayed patch antennas resonators (PARs) were first proposed in 2001.[16] PARs are ideally suited for QWIPs, as they allow illumination at normal incidence, which is clearly advantageous compared to facet illumination[6,7] while confining the electro-magnetic field inside a subwavelength volume.[16−18] Compared to QWIPs based on standard mesa geometry and of comparable collection area, this enables the realization of "thin" detectors (including a small number of quantum wells) with a higher detectivity while keeping a small capacitance, which is clearly relevant for high speed operation. QWIPs based on 2D arrays of PARs were recently demonstrated showing over 1 order of magnitude improvement in detectivity compared to a mesa reference QWIP.[19,20] However, in these works the potential in terms of high-speed operation was largely underexploited, with reported maximum heterodyne detection frequencies (no reported 3 dB bandwidth) up to only 4 GHz, limited by a device design (parasitics) leading to a large capacitance.[20] In this work we have fully addressed this issue by demonstrating PARs-based QWIP detectors specifically designed for ultrabroadband operation. Thanks to this design, we demonstrate experimentally that the detector capacitance can be reduced down to the (unavoidable) static capacitance of the antenna resonators. With these devices we demonstrate room temperature heterodyne detection at 10.3 μm with a nearly flat frequency response up to 70 GHz (limited by the detection electronics) and state of the art responsivities of ∼0.15 A/W. To the best of our knowledge, this represents the broadest experimental RF bandwidth reported to date for a QWIP detector[6,7,21] and extends by over 65 GHz the results presented in ref 20. Moreover, we develop a small-signal equivalent circuit model that can quantitively reproduce the observed device frequency response, which we find to be strongly dependent on bias and temperature. From this model we extract an RC limited 3 dB cutoff of ∼150 GHz at 300 K and an intrinsic roll-off time constant $\lesssim$1 ps, providing the first experimental evidence that QWIP detectors can indeed reach RF-bandwidths limited by electron capture on the ps time scale at room temperature. These results pave the way to the development of ultrafast MIR optoelectronics.

DEVICE DESIGN AND FABRICATION

The structure is grown by molecular beam epitaxy (MBE) on a semi-insulating GaAs substrate: 100 nm thick lattice-matched $Ga_{0.51}In_{0.49}P$ etch-stop layer followed by an $Al_{0.2}Ga_{0.8}As$/GaAs heterostructure. The PAR active region consists of seven, 6.5 nm GaAs quantum wells (QWs) with a central, 5.3 nm thick region, n-doped at a level of 6.7×10^{17} cm^{-3}. The wells width is chosen to obtain a bound-to-bound transition energy of ∼120 meV. The QWs are separated by 40 nm barriers, and the active region is sandwiched between 50 and 100 nm thick top and bottom n-doped contact layers with concentrations of 3×10^{18} cm^{-3} and 4×10^{18} cm^{-3}, respectively.

In Figure 1a,b, we present, the SEM images of the fabricated detector. It consists of a 5 × 5 periodic array of square PARs of side s = 1.85 μm and period p = 3.9 μm, sitting on top of a Ti/Au (100/400 nm) ground plane. As detailed in Spectral and dc Electrical Characterization, the values of p and s are chosen to obtain a maximum PAR array absorption as close as possible to the intersubband transition energy. At the same time, to minimize the array capacitance, the number of patches is kept to the minimum needed to allow collecting 100% of the incident radiation (∼20 μm diameter laser spotsize, see Spectral and dc Electrical Characterization).

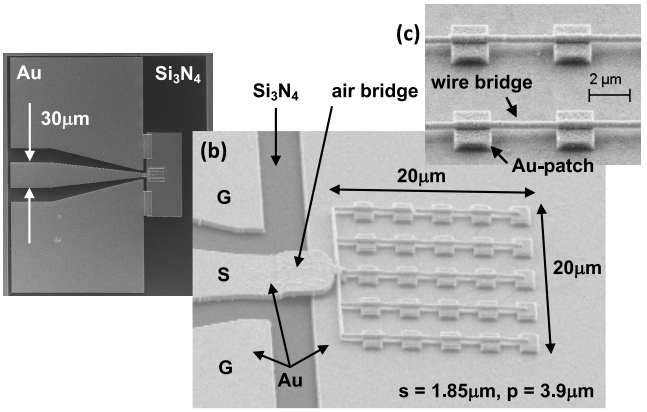

Figure 1. (a) SEM image of the 5 × 5 PAR array with an integrated coplanar waveguide. (b) Close-up on panel (a) showing the full 5 × 5 PAR array used in the experiment (s = 1.85 μm; p = 3.9 μm) and the air bridge connecting the coplanar waveguide to the array. (c) Individual resonators incorporating the multi-QW structure are connected by suspended Au wires of ∼150 nm diameter (an array with p = 5 μm is shown in the panel).

Particular care was taken in the detector microwave design, aimed at reducing the effect of parasitic capacitances brought by electrical connections and contact pads, which limited RF operation up to a few GHz in ref 20. As shown in Figure 1a,b, this is achieved by connecting the 2D array to the central electrode of a 50 Ω, tapered coplanar waveguide through an air bridge. Besides minimizing the parasitic capacitance, this solution is ideal for on-wafer testing by means of a 67 GHz microwave coplanar probe. Finally, individual resonators are connected by suspended gold wires (Figure 1b,c): compared to keeping the semiconductor beneath,[20] this solution allows minimizing the wires capacitance, while simultaneously eliminating the current flow outside the resonators, therefore reducing the dark current. As a result of our design, as shown in Heterodyne Mixing and Frequency Response, we find that the detector capacitance is essentially coincident with the static capacitance of the PARs alone, of approximately 30 fF.

The fabrication of the PARs begins with the realization of a buried metal layer serving as electromagnetic ground plane and bottom Schottky contact metallization (we have deliberately chosen Schottky rather than ohmic contacts to avoid the risk of metal diffusion in the QWIP active region due to high temperature annealing, potentially leading to high MIR losses). This is obtained by transferring the epi-layers onto a 2″-diameter high-resistivity (>5 kΩ·cm) silicon wafer using a Au−Au thermocompression bonding technique detailed in ref 22, followed by the wet etching of the GaAs substrate and the etch-stop layer. Next, the Ti/Au (8 nm/300 nm) top Schottky contact metallization is realized through e-beam lithography, followed by e-beam evaporation and lift-off. The epi-layers are subsequently ICP etched using the top metal layer as etch-mask. The ground metal layer is finally dry-etched by an Ar^+ ion-beam around the PARs array down to the silicon substrate. A 100 nm thick Si_3N_4 layer is then deposited on the silicon by plasma-enhanced chemical vapor deposition (Figure 1a,b).

To electrically connect the patches together, suspended ∼150 nm width Ti/Au (20 nm/600 nm) wire bridges are

https://dx.doi.org/10.1021/acsphotonics.0c01299
ACS Photonics 2021, 8, 464−471

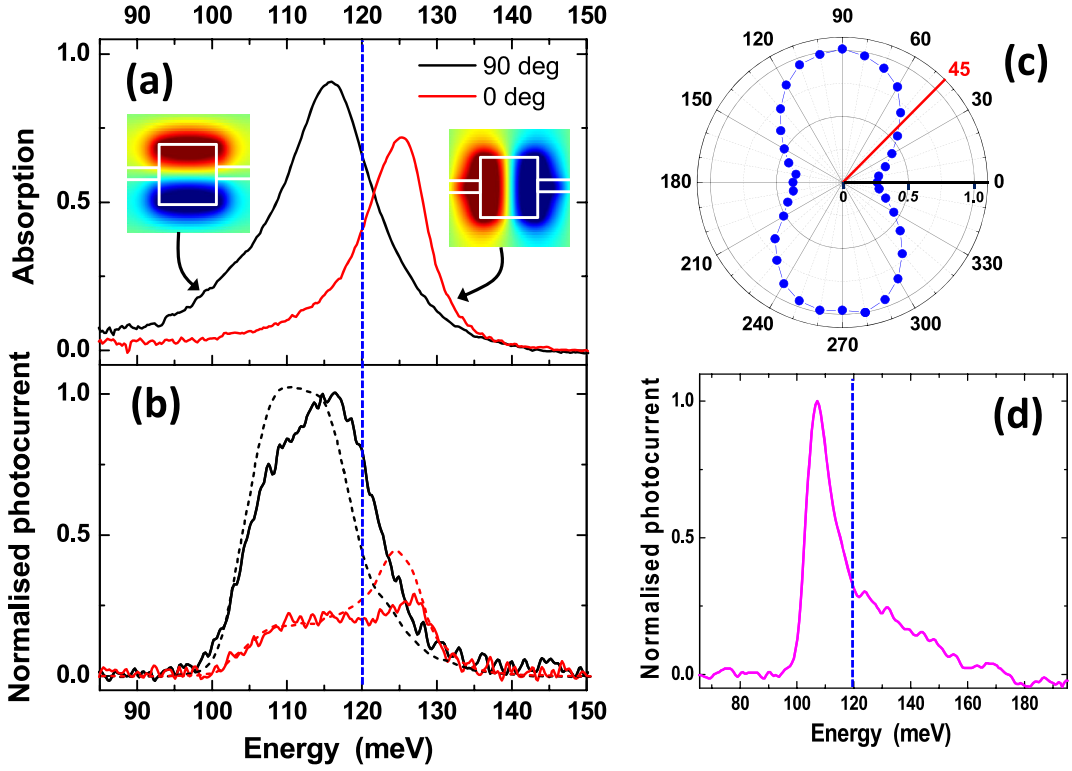

Figure 2. (a) Absorption spectra of the PARs 2D array measured at 300 K in two orthogonal polarizations: perpendicular (black) and parallel (red) to the wire bridges (spectra recorded at 77 K, not shown, are virtually identical). The measurements are performed using a MIR microscope connected to the spectrometer. (Insets) PAR fundamental modes in the two polarizations: computed 2D spatial profiles of the electric field component perpendicular to the surface (blue, positive; red, negative). Plots were obtained using a commercial FDTD solver. (b) Photocurrent spectra measured at 77 K in the two orthogonal polarizations (solid lines). Both spectra are normalized to the peak of the photocurrent spectrum at 90°. Dashed lines: spectra obtained by multiplying the spectrum of panel (d) by the absorption spectra of panel (a). (c) Normalized photocurrent vs polarization angle, measured at 300 K, with a quantum cascade laser emitting at 10.3 μm (120 meV, dashed blue lines in panels (a), (b), and (d)). The red line indicates the polarization angle (45°) used for the measurements displayed in Figures 3 and 4. (d) Photocurrent spectrum measured at 77 K (V_{bias} = 0.25 V) with the QWIP processed in a mesa geometry.

finally fabricated by a two-step e-beam lithography process. To this end, a first resist layer is used as support after deposition, e-beam lithography and reflow, followed by a second one to define the wires by standard lift-off process. The same process is used to realize the air-bridge connecting the 2D array to the 50 Ω coplanar line. The latter is deposited on the Si_3N_4: this avoids any leakage currents between the electrodes of the coplanar waveguide coming from the silicon.

SPECTRAL AND *DC* ELECTRICAL CHARACTERIZATION

In Figure 2 we report the results of the infrared spectral characterization of the PARs array. Figure 2a shows the absorption spectra at 300 K, corresponding to the fraction of the incident power absorbed by the QWIP detector with two polarizations of the incident light: orthogonal (black) and parallel (red) to the wire bridges.[19,20] The absorption is defined as $1 - R(\omega)$, where $R(\omega)$ is the reflectivity spectrum obtained through FTIR microreflectivity measurements. At the cavity resonance for the orthogonal polarization (116 meV, 10.7 μm), we find that $1 - R(\omega) = 0.9$, that is, 90% of the incident photons are absorbed. Indeed, the period p = 3.9 μm, was selected to operate the QWIP as close as possible to the critical coupling regime, compatibly with the targeted intersubband transition energy.[17] In this condition, the single PAR collection area at the resonant frequency is given by $0.9 \times p^2$, yielding a total collection area of ∼340 μm^2 (=(18.5 μm)^2) for the PAR array. As shown in the insets of Figure 2a, for the parallel polarization, the spatial distribution of the cavity mode is modified by the presence of the wire bridges, This yields a blue shift of the cavity resonance, as well as a reduced integrated absorption.

In Figure 2d, we report the measured photocurrent spectrum at 77 K, obtained by FTIR spectroscopy with the QWIP structure processed in a mesa geometry, therefore showing the effect of the bare intersubband transition. We find a peak at 107 meV, in good agreement with the expected bound-to-bound transition energy. By multiplying this spectrum by the cavity absorptions in Figure 2a, we obtain the dashed spectra shown in panel (b), in good agreement with the QWIP detector photocurrent spectra measured at 77 K, represented by the solid lines. This indicates that the PARs array absorption is dominated by absorption in the metal and contact layers (see Supporting Information for more details). From the black solid line we find that the QWIP operates in the ∼10−12 μm range, with a maximum response at ∼10.8 μm (115 meV).

In Figure 3a,b, we report the dark current and *dc* photocurrent vs bias characteristics at 77 and 300 K, obtained by illuminating the QWIP with a 10.3 μm (120 meV) DFB quantum cascade laser (QCL), polarized at 45° with respect to the wire bridges (the full polarization dependence at 77 K is reported in Figure 2c). For these measurements, the collimated beam from the QCL was focused on the detector using an AR

https://dx.doi.org/10.1021/acsphotonics.0c01299
ACS Photonics 2021, 8, 464−471

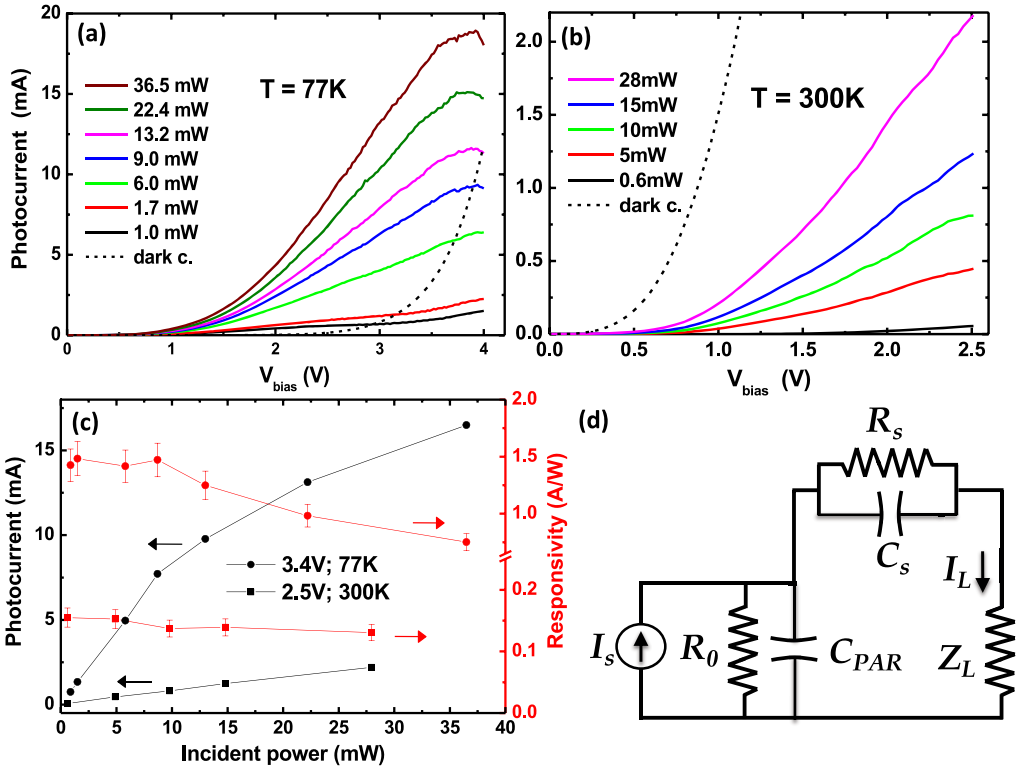

Figure 3. Photocurrent vs applied bias at (a) 77 and (b) 300 K for different incident QCL powers. The dark current I/V characteristics are shown in dashed. (c) Photocurrents (black dots) and responsivities (red dots) vs power, measured at 2.5 V, 300 K (squares) and 3.4 V, 77 K (circles). (d) Small signal; equivalent circuit of the QWIP detector (see text). $C_{PAR} \sim 30$ fF and $C_s \sim 1$ pF are, respectively, the 2D PARs array and Schottky contact capacitances. R_0 and R_s (see Table 1) are, respectively, the *dc* internal photoresistance of the PARs array, and the leakage resistance of the Schottky contact biased in reverse breakdown, both under illumination (the forward biased Schottky junction is considered as a short circuit). $Z_L \sim 50\ \Omega$ is the load impedance seen by the QWIP.

coated aspheric lens (NA = 0.56; 5 mm focal length). At 10.3 μm we measured a waist diameter of 20 μm using a knife-edge technique, that is, approximately equal to the side of the 5 × 5 PAR array collection area (18.5 μm ∼ $\sqrt{340\ \mu m^2}$). Therefore, for the rest of this work, we assume that all the QCL power, measured after the lens, is incident on the QWIP. This corresponds to the power values reported in Figure 3a,b.

As expected, at 300 K, the dark current dominates the photocurrent for all power levels. At 77 K, the situation is reversed, showing that, at this temperature, the QWIP can be potentially operated in the photon-noise regime with only a few mW of incident power.[2] At 77 K and 3.5−4 V (Figure 3a), we observe a pronounced saturation of the photocurrent that we attribute to negative differential drift velocity, resulting from intervalley scattering.[23] Saturation fields in the 10−20 kV/cm range have been found in previous works. Here, at 3.9 V (Figure 3a), the average electric field is ∼100 kV/cm, indicating that a large fraction of the applied bias drops on the Schottky contacts.

The photocurrent and responsivity as a function of incident power at 77 and 300 K are reported in Figure 3c, respectively, at 3.4 and 2.5 V. Responsivities are corrected by the polarization factor (Figure 2c), and their value corresponds to the situation where the incident field is polarized orthogonally to the wires, which is the ideal condition to operate the QWIP. At low power, we obtain responsivities R = 1.5 and 0.15 A/W at 77 and 300 K. From the reflectivity spectrum of Figure 2a (black line) and assuming an intersubband transition energy centered at 107 meV with a fwhm of 10% (see the spectrum of Figure 1d), we find that the responsivity measured at 77 K at high bias and low optical power is compatible with a photoconductive gain $g = \tau_c/\tau_{tr} \cong 2.5$, where τ_c and τ_{tr} are, respectively, the electron's capture and transit time (see Supporting Information).[24] The decrease of responsivity at 300 K is attributed to a decrease in the drift velocity and capture time (see Table 1). Finally, by increasing the power we observe a clear decrease of responsivity at 77 K. This is attributed to the presence of a series resistance provided by the Schottky contacts (R_S in the circuit of Figure 3d, see Heterodyne Mixing and Frequency Response and Table 1). As a consequence, for a given applied bias, the decrease of the detector photoresistance (R_0 in the circuit of Figure 3d) with increasing incident power produces a progressive lowering of the electric field across the QWIP active region.[25] At room temperature, R_s is instead negligible (see Table 1); therefore, the saturation effect is much less pronounced.

HETERODYNE MIXING AND FREQUENCY RESPONSE

In Figure 4 we report the heterodyne frequency response (FR) of the QWIP in the 10 MHz−67 GHz range, measured at 77 and 300 K, at low and high applied biases. To record these spectra, we used a 67 GHz-bandwidth cryogenic probe, positioned at the edge of the coplanar waveguide shown in Figure 1a. The photodetector was connected to a wideband

https://dx.doi.org/10.1021/acsphotonics.0c01299
ACS Photonics 2021, 8, 464−471

Table 1. Measured Photocurrents (I_{ph}), I_0, and Small-Signal Circuit Resistances under Illumination (R_0, R_s) Used To Compute the Solid Lines in Figure 4 for Different Operating Conditions (Bias and Temperature)[a]

T(K)	77	300	77	300
V_{bias}(V)	1.1	0.9	3.4	2.5
I_{ph}(mA)	0.49	0.14	15.2	2.2
I_0(mA)	0.49	0.38	15.2	2.2
R_0(Ω)	200	75	40	40
R_s(Ω)	350	125	20	0
τ(ps)	1.5	≲1	8	2.5
τ_c(ps)	1	≲1	10	2.5
τ_{tr}(ps)	25	90	8	14
v_d (x10⁶cm/s)	1.5	≳0.4	4.6	2.6

[a]The value of the roll-off time constant (τ in eq 1) is the one yielding the best fit of the experimental data. The capture time (τ_c) and transit time (τ_{tr}) are obtained from τ and the photoconductive gain (see text). The corresponding drift velocity (v_d) is obtained from the ratio between the thickness of the QWIP active region (365 nm) and τ_{tr}.

bias-T and simultaneously illuminated by two 10.3 μm wavelength DFB QCLs driven with ultralow noise (~300 pA/Hz$^{1/2}$) current generators (see Supporting Information for a schematic of the experimental setup). The current of one QCL was kept constant while the current and temperature of the second one were fine-tuned in order to sweep the heterodyne frequency in the range 0−67 GHz. The powers incident on the QWIP from the two QCLs are P_1 = 27.5 mW and P_2 = 6 mW (33.5 mW total). The spectra of Figure 4 correspond to the intensities of the heterodyne beat signals recorded with a spectrum analyzer (SA) set in max-hold trace mode. The traces are corrected by (i) the propagation losses from the QWIP to the SA measured with a vector network analyzer (VNA) and (ii) the power changes (2 dB max) of one QCL due to temperature/current tuning (see Supporting Information).

The top two traces in Figure 4 show the detector FR at high bias, that is, 3.4 V (77 K) and 2.5 V (300 K). From Figure 2c, the corresponding responsivities are 0.75 A/W and 0.13 A/W. At 77 K, we find a monotonic decrease with frequency, with a 3 dB-cutoff frequency of ~30 GHz, while at 300 K, the response is much flatter, with a ~2 dB increase from 0 to ~40 GHz, followed by a 3 dB drop at ~67 GHz.

At low biases the shape of the FR is rather different. As shown by the two bottom traces, recorded at 1.1 V (77 K) and 0.9 V (300 K), the FR is virtually flat up to 67 GHz, except at low frequencies where we observe a pronounced drop below ~5 GHz (77 K) and ~10 GHz (300 K).

To gain insight in the behavior of the QWIP, we used a VNA analyzer to derive the device impedance vs frequency in the operating conditions corresponding to the spectra of Figure 4. We find that at low bias (1.1 V and 0.9 V spectra in Figure 4) the detector's RF impedance can be well reproduced using the simple small-signal circuit displayed in Figure 3d (see Supporting Information for the for the complete derivation of the circuit parameters).[26] Here R_0, R_s, and Z_L ~ 50 Ω represent (i) the *dc* internal photoresistance of the 5 × 5 PAR array

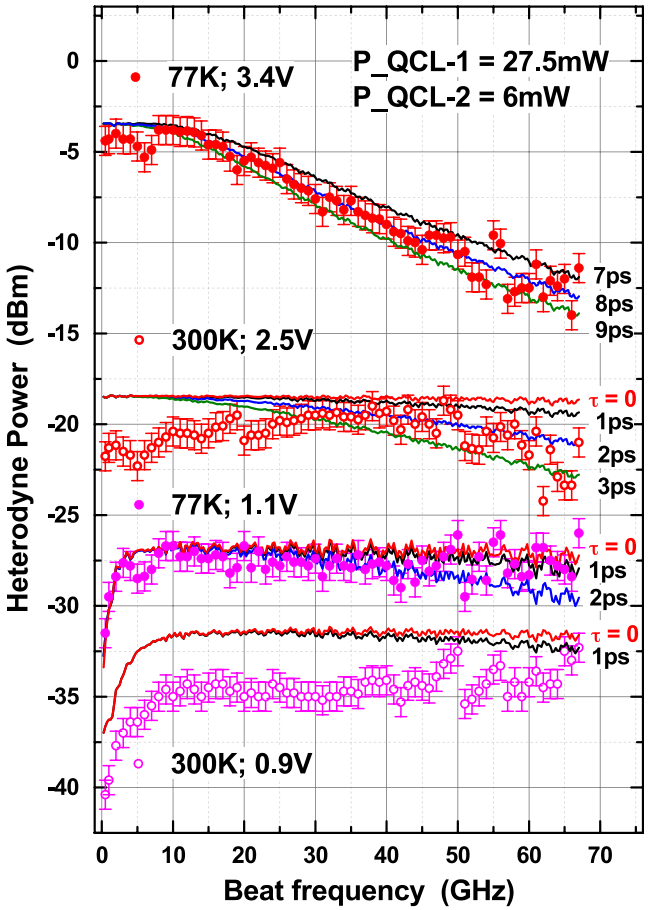

Figure 4. QWIP detector FRs at different temperatures and biases (dotted curves). The powers incident on the QWIP from the two QCLs are P_1 = 27.5 mW and P_2 = 6 mW (33.5 mW total). The spectra are corrected by the attenuation from the QWIP to the SA, measured with a VNA analyzer. The solid lines correspond to fits obtained using the small-signal circuit model of Figure 3d for different carrier's lifetimes (see main text).

under illumination, (ii) the resistance of the reverse biased Schottky contact under illumination (the forward biased Schottky junction is considered as a short circuit), and (iii) the measured load impedance seen by the QWIP detector. C_{PAR} ~ 30 fF and C_s ~ 1 pF are, respectively, the 2D PARs array and Schottky contact capacitance. The former corresponds to the computed static capacitance of the PARs array.

The current source in the circuit represents the photocurrent generated in the patch array oscillating at the beat frequency ω_b. It is given by

$$I_s = \frac{m}{\sqrt{1 + (\omega_b\tau)^2}} I_{ph} \frac{R_d + R_s}{R_d} = \frac{m}{\sqrt{1 + (\omega_b\tau)^2}} I_0 \quad (1)$$

where m is a modulation index given by $m = \frac{2\sqrt{P_1 \times P_2}}{P_1 + P_2} = 0.77$, I_{ph} is the *dc* (i.e., average) measured photocurrent, R_d is the PARs array dark resistance, and $I_0 = I_{ph}(R_d + R_s)/R_d$. The term under the square root at the denominator takes into account the frequency roll-off of the intrinsic transport mechanism, with τ approximating the carriers capture or transit time.[24,26] Concerning R_d, based on the fact that at 77 K (300 K) the QWIP current under illumination is dominated by the photocurrent (dark current) component (see Figure 3a,b),

https://dx.doi.org/10.1021/acsphotonics.0c01299
ACS Photonics 2021, 8, 464−471

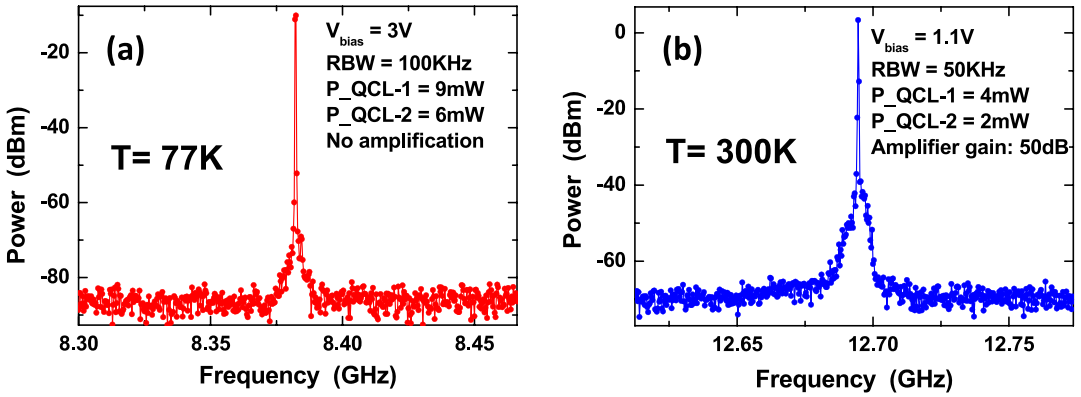

Figure 5. Examples of single shot heterodyne beatnote spectra recorded (a) at 77 K without amplification and (b) at 300 K with a low noise, narrow band amplifier of 50 dB gain.

we have made the following approximations: $R_d \approx R_0$ at 300 K, and $R_d \gg R_s$ at 77 K. These approximations allow de facto to eliminate the QWIP dark resistance as an independent variable from the source term in eq 1 (see Supporting Information for more details).

The solid curves corresponding to the two bottom FRs in Figure 4 represent the power dissipated in the load: $P_L = \frac{1}{2}\mathcal{R}e[Z_L]\cdot|I_L|^2$. They are computed from the circuit of Figure 3d (with eq 1 for I_s) using (i) $R_0 = 200\ \Omega$, $R_s = 350\ \Omega$, for the spectrum at 1.1 V (77 K) with $I_{ph} = 0.49$ mA and $\tau = 1-2$ ps; and (ii) $R_0 = 75\ \Omega$, $R_s = 125\ \Omega$, for the spectrum at 0.9 V (300 K), with $I_{ph} = 0.14$ mA and $\tau \sim 1$ ps (see Table 1, first and second column). Despite the fairly simple electrical model and the measurement uncertainties the agreement with the experimental FRs is very good, both in terms of absolute power and spectral shape. In particular, the observed drop at low frequency reflects the additional conversion losses due to the heterodyne power dissipated in R_s when $f_b \lesssim (2\pi R_s C_s)^{-1}$ (see Figure 3.d). At higher frequencies, R_s is instead shorted by C_s, thus eliminating the power loss in the contact resistance. In this case, from the small-signal circuit model, we have that

$$I_L = I_s \frac{1}{1 + R_L/R_0 + i\omega_b R_L C_{PAR}} \quad (2)$$

yielding a parasitic roll-off time constant $R_L C_{PAR}/(1 + R_L/R_0) \lesssim 1$ ps (see Table 1). We also find (see Supporting Information) that, for the chosen PAR array size, the QWIP impedance at low bias is close to 50 Ω for frequencies ≳20 GHz (300 K) and 30 GHz (77 K), which is ideal for RF impedance matching.

At high biases, the effect of C_s is much less pronounced and the power drop at low frequencies disappears (Figure 4, top two spectra). From the small-signal circuit, this can be explained by a reduction of R_s due to the Schottky barrier becoming more transparent, therefore, effectively shunting C_s at low frequencies. As a result, the QWIP impedance does not display the strong increase at low frequency found at low biases (see Supporting Information). From the small-signal circuit we find a good agreement with the measured FRs using (i) $R_0 = 40\ \Omega$, $R_s = 20\ \Omega$, for the spectrum at 3.4 V (77 K), with $\tau \sim 8$ ps and $I_{ph} = 15.2$ mA; and (ii) $R_0 = 40\ \Omega$, $R_s = 0\ \Omega$, for the spectrum at 2.5 V (300 K), with $\tau \sim 2-3$ ps and $I_{ph} = 2.2$ mA (see Table 1, third and fourth columns). As a result, at 300 K the QWIP is almost impedance matched to 50Ω at all frequencies. We note that our small signal circuit model does not explain the ∼2 dB increase in the FR from 0 to ∼40 GHz observed at 2.5 V.

As shown above, thanks to the very small device capacitance, by fitting the measured FRs using the small signal circuit model, we can extract the intrinsic detector response times that, as shown by the solid curves in Figure 4, are dependent on the operating conditions. From the values of τ and from the photoconductive gain derived from the responsivities, we can then obtain the values of τ_c and τ_{tr} shown in Table 1 (see Supporting Information): except at 77 K under high bias, the QWIP intrinsic response time appears to be dominated by electron capture. We also find the expected decrease/increase of τ_{tr} with increasing bias/temperature.[24] Interpreting the dependence of τ_c on bias and temperature is beyond the scope of this work and will require more systematic measurements that are presently under way. At the same time, on this subject there appears to be a lack of experimental data in the literature.[4]

In Figure 5 we report two examples of heterodyne beatnote spectra recorded in single shot at 77 K, under an applied bias of 3 V and without any amplification (Figure 5a), and at 300 K, with an applied bias of 1.1 V and with a narrow band amplifier of 50 dB gain (Figure 5b). In the first case, the noise floor is limited by the spectrum analyzer, while in the second spectrum the noise floor is determined by the amplifiers noise. We find instantaneous line widths of ∼100 kHz, limited by the QCL thermal and current fluctuations. At 77 K, the RBW is set to 100 kHz, yielding a SNR of ∼77 dB, while at 300 K, we find a SNR of 72 dB with a RBW of 50 kHz. Reducing further the RBW produces a decrease of the beatnote intensity because the RBW goes below the instantaneous heterodyne beatnote line width.

The dependence of the SNR of the heterodyne beatnote frequency, obtained with the spectrum analyzer without amplification ($P_1 = 27.5$ mW and $P_2 = 6$ mW), can be directly extracted from the spectra recorded in max-hold trace mode (see Supporting Information). At 30 and 60 GHz, with a RBW of 3.5 MHz, we obtain SNRs of 50 and 35 dB and of 35 and 25 dB, respectively, at 77 K (3.4 V) and 300 K (2.5 V).

CONCLUSIONS

Antenna-coupled QWIP detectors operating in the 10−12 μm range are demonstrated, exhibiting a flat frequency response up to 67 GHz at 77 K and 300 K. At 300 K, from our experimental results and with the help of an equivalent circuit model, we find an RC-limited 3 dB cutoff frequency >150 GHz

https://dx.doi.org/10.1021/acsphotonics.0c01299
ACS Photonics 2021, 8, 464−471

and ∼ps intrinsic response times. These results are achieved thanks to a detector specifically designed for ultrafast operation and provide the first experimental evidence that QWIPs can indeed reach RF-bandwidths limited by electron capture over time scales of ∼1 ps at room temperature.

We believe that the detectors demonstrated here, in combination with QCLs, will open up new perspectives in MIR photonics, namely, by extending to the MIR range, the possibilities offered by ultrafast near-infrared optoelectronics, so far the only frequency range benefiting from the availability of ultrafast photodetectors. Envisaged applications are free space communications with data rates >10Gb/s, coherent multispecies gas sensing, high precision spectroscopy and metrology, and astronomy, as well as to study real-time dynamics on the 10 ps time scale.[8−11,27] More specifically, on this last topic, we expect that broadband devices, such as those demonstrated in this work, can shed new light on the ultrafast electron's dynamics in QWIPs.

A final intriguing perspective is the use of these structures as QCL-pumped photomixers for the generation of sub-THz radiation.[28,29] To this end, we note that the actual responsivity of ∼0.75 A/W at 77 K, 3.4 V (high power, see Figure 3c) could be theoretically brought up to ∼4 A/W if the ISB transition peak and the PAR resonance were perfectly matched. In this case, from the top trace in Figure 4, we would expect microwave power levels in the mW range. Replacing the Schottky contacts with nondiffusive ohmic contacts (not to increase MIR photon absorption) should also reduce the saturation of the responsivity at high incident powers (Figure 2c, 77 K).

■ ASSOCIATED CONTENT

Supporting Information

The Supporting Information is available free of charge at https://pubs.acs.org/doi/10.1021/acsphotonics.0c01299.

Computed responsivity; Circuit model; Heterodyne mixing experimental setup and frequency response spectra; QWIP impedance measurements; Determination of QWIP circuit parameters; Evaluation of carriers capture and transit time (PDF)

■ AUTHOR INFORMATION

Corresponding Author

Stefano Barbieri − *Institute of Electronics, Microelectronics and Nanotechnology, Univ. Lille, ISEN, CNRS, UMR 8520, 59652 Villeneuve d'Ascq, France*; orcid.org/0000-0003-4024-8898; Email: stefano.barbieri@univ-lille.fr

Authors

Michael Hakl − *Institute of Electronics, Microelectronics and Nanotechnology, Univ. Lille, ISEN, CNRS, UMR 8520, 59652 Villeneuve d'Ascq, France*

Quyang Lin − *Institute of Electronics, Microelectronics and Nanotechnology, Univ. Lille, ISEN, CNRS, UMR 8520, 59652 Villeneuve d'Ascq, France*

Sylvie Lepillet − *Institute of Electronics, Microelectronics and Nanotechnology, Univ. Lille, ISEN, CNRS, UMR 8520, 59652 Villeneuve d'Ascq, France*

Maximilien Billet − *Institute of Electronics, Microelectronics and Nanotechnology, Univ. Lille, ISEN, CNRS, UMR 8520, 59652 Villeneuve d'Ascq, France*

Jean-François Lampin − *Institute of Electronics, Microelectronics and Nanotechnology, Univ. Lille, ISEN, CNRS, UMR 8520, 59652 Villeneuve d'Ascq, France*

Stefano Pirotta − *Centre de Nanosciences et de Nanotechnologies (C2N), CNRS UMR 9001, Université Paris-Saclay, 91120 Palaiseau, France*

Raffaele Colombelli − *Centre de Nanosciences et de Nanotechnologies (C2N), CNRS UMR 9001, Université Paris-Saclay, 91120 Palaiseau, France*

Wenjian Wan − *Key Laboratory of Terahertz Solid State Technology, Chinese Academy of Sciences, Shanghai 200050, China*

J. C. Cao − *Key Laboratory of Terahertz Solid State Technology, Chinese Academy of Sciences, Shanghai 200050, China*

Hua Li − *Key Laboratory of Terahertz Solid State Technology, Chinese Academy of Sciences, Shanghai 200050, China*; orcid.org/0000-0003-3689-2437

Emilien Peytavit − *Institute of Electronics, Microelectronics and Nanotechnology, Univ. Lille, ISEN, CNRS, UMR 8520, 59652 Villeneuve d'Ascq, France*

Complete contact information is available at: https://pubs.acs.org/10.1021/acsphotonics.0c01299

Author Contributions

‡M.H. and Q.L. contributed equally to the work. M.H. made the electromagnetic simulations of the patch antenna array with contributions from R.C. and S.B. E.P. designed the coplanar waveguide. W.W., H.L., and J.C.C. performed the sample growth. Q.L. fabricated the samples under the supervision of E.P. M.B. contributed to the sample fabrication. S.P. and R.C. measured the QWIP reflectivity and photocurrent spectra. M.H. and S.B. built the experimental setup for the measurement of the QWIP *dc* photocurrent and *ac* frequency response. J.L. contributed to the experimental setup. M.H., Q.L., S.L., and S.B. performed the measurement of the QWIP *dc* photocurrent and *ac* frequency response. S.L. performed the measurements of the S-parameters. E.P. and S.B. derived the equivalent circuit model and fitted the data with contributions from J.L. M.H., Q.L., J.L., R.C., H.L., E.P., and S.B. discussed and analyzed the results. S.B. wrote the manuscript with contributions from M.H., Q.L., E.P., J.L., R.C., and H.L. E.P. and S.B. supervised the project.

Funding

Nord-Pas de Calais Regional Council; Fonds Européens de Développement Régional. RENATECH (French Network of Major Technology Centres); CPER "Photonics for Society"; French National Research Agency, and Direction Générale de l'Armement (Project HISPANID); French National Research Agency (Project IRENA); European Union FET-Open Grant MIR-BOSE (737017) and the European Research Council (IDEASERC; "GEM"; 306661); National Natural Science Foundation of China (61875220); "From 0 to 1" Innovation Program of the Chinese Academy of Sciences (ZDBS-LY-JSC009).

Notes

The authors declare no competing financial interest.

■ REFERENCES

(1) Bethea, C. G.; Levine, F.; Hasnain, G.; Walker, J.; Malik, R. J. High-speed measurement of the response time of a GaAs/$Al_xGa_{1-x}As$

multiquantum-well long-wavelength infrared detector. *J. Appl. Phys.* **1989**, *66*, 963.
(2) Liu, H. C.; Li, J.; Brown, E. R.; McIntosh, K. A.; Nichols, K. B.; Manfra, M. J. Quantum Well Intersubband Heterodyne Infrared Detection Up to 82 GHz. *Appl. Phys. Lett.* **1995**, *67*, 1594.
(3) Ehret, S.; Schneider, H.; Fleissner, J.; Koidl, P.; Bohm, G. Ultrafast intersubband photocurrent response in quantum-well infrared photodetectors. *Appl. Phys. Lett.* **1997**, *71*, 641.
(4) Steinkogler, S.; Schneider, H.; Rehm, R.; Walther, M.; Koidl, P.; Grant, P.; Dudek, R.; Liu, H. C. Time-resolved electron transport studies on InGaAs/GaAs-QWIPs. *Infrared Phys. Technol.* **2003**, *44*, 355.
(5) Steinkogler, S.; Schneider, H.; Walther, M.; Koidl, P. Determination of the electron capture time in quantum-well infrared photodetectors using time-resolved photocurrent measurement. *Appl. Phys. Lett.* **2003**, *82*, 3925.
(6) Grant, P. D.; Dudek, R.; Buchanan, M.; Wolfson, L.; Liu, H. C. An ultrafast quantum well infrared photodetector. *Infrared Phys. Technol.* **2005**, *47*, 144.
(7) Grant, P. D.; Dudek, R.; Buchanan, M.; Liu, H. C. Room-temperature heterodyne detection up to 110 GHz with a quantum well infrared photodetector. *IEEE Photonics Technol. Lett.* **2006**, *18*, 2218.
(8) Pang, X.; Ozolins, O.; Schatz, R.; Storck, J.; Udalcovs, A.; Navarro, J. R.; Kakkar, A.; Maisons, G.; Carras, M.; Jacobsen, G.; Popov, S.; Lourdudoss, S. Gigabit free-space multi-level signal transmission with a mid-infrared quantum cascade laser operating at room temperature. *Opt. Lett.* **2017**, *42*, 3646.
(9) Liu, J. J.; Stann, B. L.; Klett, K. K.; Cho, P. S.; Pellegrino, P. M. Mid and Long-Wave Infrared Free-Space Optical Communication. *Proc. SPIE* **2019**, *11133*, 1113302−1.
(10) Macleod, N. A.; Molero, F.; Weidmann, D. Broadband standoff detection of large molecules by mid-infrared active coherent laser spectrometry. *Opt. Express* **2015**, *23*, 912.
(11) Weidmann, D.; Reburn, W. J.; Smith, K. M. Ground-based prototype quantum cascade laser heterodyne radiometer for atmospheric studies. *Rev. Sci. Instrum.* **2007**, *78*, 073017.
(12) Brown, E. R.; McIntosh, K. A.; Nichols, K. B.; Smith, F. W.; Manfra, M. J. CO_2-Laser Heterodyne Detection with GaAs/AlGaAs MQW Structures, in Quantum Well Intersubband Transition Physics and Devices. *NATO ASI Series*; Springer, 1994; pp 207−220.
(13) Grossman, E. N.; Sauvageau, J. E.; McDonald, D. G. Lithographic spiral antennas at short wavelengths. *Appl. Phys. Lett.* **1991**, *59*, 3225.
(14) Chong, N.; Ahmed, H. Antenna-coupled polycrystalline silicon air- bridge thermal detector for mid-infrared radiation. *Appl. Phys. Lett.* **1997**, *71*, 1607.
(15) González, F. J.; Ilic, B.; Alda, J.; Boreman, G. D. Antenna-Coupled Infrared Detectors for Imaging Applications. *IEEE J. Sel. Top. Quantum Electron.* **2005**, *11*, 117.
(16) Beck, A.; Mirotznik, M. S. Microstrip antenna coupling for quantum-well infrared photodetectors. *Infrared Phys. Technol.* **2001**, *42*, 189.
(17) Palaferri, D.; Todorov, Y.; Mottaghizadeh, A.; Frucci, G.; Biasiol, G.; Sirtori, C. Ultra-subwavelength resonators for high temperature high performance quantum detectors. *New J. Phys.* **2016**, *18*, 113016.
(18) Le Perchec, J.; Desieres, Y.; Espiau de Lamaestre, R. Plasmon-based photosensors comprising a very thin semiconducting region. *Appl. Phys. Lett.* **2009**, *94*, 181104.
(19) Chen, Y. N.; Todorov, Y.; Askenazi, B.; Vasanelli, A.; Biasiol, G.; Colombelli, R.; Sirtori, C. Antenna-coupled microcavities for enhanced infrared photo-detection. *Appl. Phys. Lett.* **2014**, *104*, 031113−1.
(20) Palaferri, D.; Todorov, Y.; Bigioli, A.; Mottaghizadeh, A.; Gacemi, D.; Calabrese, A.; Vasanelli, A.; Li, L.; Davies, A. G.; linfield, E. H.; Kapsalidis, F.; Beck, M.; Faist, J.; Sirtori, C. Room-temperature 9-μm wavelength photo- detectors and GHz-frequency heterodyne receivers. *Nature* **2018**, *556*, 85.
(21) Rodriguez, E.; Mottaghizadeh, A.; Gacemi, D.; Palaferri, D.; Asghari, Z.; Jeannin, M.; Vasanelli, A.; Bigioli, A.; Todorov, Y.; Beck, M.; Faist, J.; Wang, Q. J.; Sirtori, C. Room temperature, wide-band Quantum Well Infrared Photodetector for microwave optical links at 4.9 μm wavelength. *ACS Photonics* **2018**, *5*, 3689.
(22) Peytavit, E.; Lampin, J.-F.; Hindle, F.; Yang, C.; Mouret, G. Wide-band continuous-wave terahertz source with a vertically integrated photomixer. *Appl. Phys. Lett.* **2009**, *95*, 161102.
(23) Schneider, H.; Mermelstein, C.; Rehm, R.; Schönbein, C.; Sa'ar, A.; Walther, M. Optically induced electric-field domains by bound-to-continuum transitions in n-type multiple quantum wells. *Phys. Rev. B: Condens. Matter Mater. Phys.* **1998**, *57*, R15096.
(24) Schneider, H.; Liu, H. C. *Quantum Well Infrared Photodetectors: Physics and Applications*; Springer, 2007; pp 72−75.
(25) Ershov, M.; Liu, H. C.; Buchanan, M.; Wasilewski, Z. R.; Ryzhii, V. Photoconductivity nonlinearity at high excitation power in quantum well infrared photodetectors. *Appl. Phys. Lett.* **1997**, *70*, 414.
(26) Coleman, P. D.; Eden, R. C.; Weaver, J. N. Mixing and Detection of Coherent Light, IEEE Trans. *IEEE Trans. Electron Devices* **1964**, *11*, 488.
(27) Hale, D. D.S.; Bester, M.; Danchi, W. C.; Fitelson, W.; Hoss, S.; Lipman, E. A.; Monnier, J. D.; Tuthill, P. G.; Townes, C. H. The Berkeley infrared spatial interferometer: a heterodyne stellar interferometer for the mid-infrared. *Astrophys. J.* **2000**, *537*, 998.
(28) Peytavit, E.; Lepilliet, S.; Hindle, F.; Coinon, C.; Akalin, T.; Ducournau, G.; Mouret, G.; Lampin, J.-F. Milliwatt-level output power in the sub-terahertz range generated by photomixing in a GaAs photoconductor. *Appl. Phys. Lett.* **2011**, *99*, 223508.
(29) Peytavit, E.; Latzel, P.; Pavanello, F.; Ducournau, G.; Lampin, J.-F. CW Source Based on Photomixing With Output Power Reaching 1.8 mW at 250 GHz, IEEE Electron. *IEEE Electron Device Lett.* **2013**, *34*, 1277.

https://dx.doi.org/10.1021/acsphotonics.0c01299
ACS Photonics 2021, 8, 464−471